

Analytical design criteria for realizing ideal standard filters in strongly coupled resonant systems, with application to microwave metasurfaces

Mohammed Benzaouia ^{1,*}, John D. Joannopoulos,² Steven G. Johnson ³ and Aristeidis Karalis ^{4,†}

¹*Department of Electrical Engineering and Computer Science,
Massachusetts Institute of Technology, Cambridge, MA 02139, USA.*

²*Department of Physics, Massachusetts Institute of Technology, Cambridge, MA 02139, USA.*

³*Department of Mathematics, Massachusetts Institute of Technology, Cambridge, MA 02139, USA.*

⁴*Research Laboratory of Electronics, Massachusetts Institute of Technology, Cambridge, MA 02139, USA.*

We present general analytical criteria for the precise design of lossless reciprocal 2-port systems verifying $S_{22} = e^{i\varphi} S_{11}$, including symmetric ($S_{22} = S_{11}$) or “antimetric” ($S_{22} = -S_{11}$) ideal standard filters (Chebyshev, elliptic, etc.). We show that the non-normalized resonant (quasi-normal) modes (QNMs) of all such 2-port systems couple to the input and output ports with specific unitary ratios, whose relative signs determine the position of the scattering zeros. This allows us to obtain design criteria assigning values to the poles, background response, and QNM-to-ports coupling coefficients. Filter devices can then be designed via a well-conditioned nonlinear optimization (or root-finding) problem using a numerical eigensolver. As an application, we design microwave metasurface filters that precisely match standard bandpass or bandstop filters of various types, orders and bandwidths, with focus on the best-performing elliptic filters.

I. INTRODUCTION

High-order (multi-resonance) filters—especially ideal standard filters (ISFs), such as Butterworth or elliptic [1]—have been designed for many types of wave physics (electromagnetic [2–12], mechanical [13–17], etc.) by a variety of techniques, including brute-force optimization of the transmission/scattering spectrum [18–21], circuit theory in the microwave regime [22–31], and coupled-mode theory (CMT) [32–34] for cascaded optical resonators [2–8]. Circuit theory and CMT provide attractive semi-analytical frameworks for filter design, but are restricted to systems composed of spatially separable components (either discrete circuit elements or weakly coupled resonances, respectively), while brute-force spectrum optimization faces several numerical challenges. To design ultra-compact filters, involving strongly coupled elements and spatially overlapping resonances, a precise, systematic and computationally tractable methodology is missing. In this article, we develop a new such filter-design approach by deriving a minimal set of explicit *analytical* criteria on the system resonances, applicable to all symmetric and “antimetric” [35] filters, including ISFs. To derive these conditions, we use the unitary and symmetric quasi-normal-mode (QNM) expansion of the scattering matrix S from Ref. 36 to derive the required coupling coefficients of the resonances (QNMs) to the input and output ports in conjunction with the net background response, in order to achieve multiple configurations for the zeros of the S coefficients (generalizing previous work [37, 38]) and thus realize any desired ISF. We apply our procedure to computationally design microwave metasurface filters that precisely match ISFs of

various orders, bandwidths, and types—especially optimal elliptic filters, which were demonstrated only approximately in the past [21–25].

Large-scale optimization (including a variety of inverse-design and machine-learning algorithms) is a powerful approach to design complex structures by optimizing thousands of degrees of freedom [39, 40]. However, if the optimization problem is formulated directly in terms of matching a desired transmission spectrum, it can face severe numerical challenges: the highly oscillatory nature of the transmission spectrum can trap optimizers in poor local optima, and stringent constraints (e.g. on stop- and pass-band transmission) can lead to very “stiff” optimization problems with slow convergence. (One proposed solution was to restrict the designs to spatially distinct resonators as in CMT [41].) However, when analytical solutions to *parts* of the problem exist, the numerical side of the optimization can be rendered simpler and more robust. For filter design in particular, signal-processing theory analytically defines many such “optimal” filters (ISFs), characterized by various rational transfer functions with specified poles and zeros, the latter necessary to achieve a steep transition between the “pass” and “stop” frequency bands. Therefore, when designing physical filters, it is advantageous to exploit these analytical solutions. An exact methodology, called network synthesis, was developed to implement these ISFs in the extreme quasi-static (subwavelength) limit, where structures can be modeled precisely by networks of discrete elements, as in electronic circuits [1]. In the other limit of structures spanning multiple wavelengths, the simple mapping between coupled resonators and transfer-function poles has made temporal coupled-mode theory (CMT) [32–34] a popular design tool, especially for (high-order) optical add-drop filters [2–7], most of which are only Chebyshev or Butterworth filters with no transmission-zeros, using a symmetric topology. However, in the intermediate limit of physical struc-

* Corresponding author: medbenz@mit.edu

† Corresponding author: aristos@mit.edu

tures with size on the order of the wavelength or only a few times smaller (metamaterials), no complete filter-design methodology exists. Discrete-element equivalent networks must often become overly complicated to model the full-wave physics accurately and they change for each different structural topology [29] or, worse, they fail to provide any adequate model (as is typically the case in dielectric photonic structures). Therefore, network synthesis may be useful for the intuitive choice of an appropriate system topology but not for the calculation of its exact parameters. CMT, on the other hand, is typically based on weakly coupled resonators and the knowledge of the “uncoupled” modes of the system [34], but neither of these conditions usually hold for wavelength-scale structures with multiple strongly inter-coupled/overlapping resonances [42]. Still missing has been a unified, physics-independent, set of exact conditions for the precise design of filters with multiple zeros that can be fed as a smooth objective to optimization algorithms. Using our QNM theory (QNMT) of Ref. 36 (whose main results are summarized in Sec. II), in Sec. III we derive such simple and general rules to design ISFs using eigenmode solvers. In particular, we show that the resonant QNM fields of *all* lossless reciprocal 2-port systems with symmetric ($S_{22} = S_{11}$) or “antimetric” ($S_{22} = -S_{11}$) [35] response couple to the input and output ports with specific unitary ratios, whose relative signs determine the position of the scattering zeros. Thus, for filter design, apart from the obvious matching of system resonant frequencies to the desired filter’s complex poles, we explain that, to also obtain the desired-filter zeros, these ratios must be enforced for the critical filter resonances and the remaining QNMs must add up to a required overall background response.

As an application of our theory, we design microwave frequency selective surfaces (FSS), which are usually used to implement spatial (wave) filters for communication antennas, radars, radomes [10–12], lenses [43, 44] etc. FSSs typically take the form of two-dimensional periodic metal-dielectric arrays exhibiting specific frequency-dependent transmission or reflection under planewave excitation. While older designs were based on wavelength-sized unit cells (as in typical antenna design), the use of subwavelength dimensions to form metasurfaces has attracted much attention in the past decade due to multiple advantages, such as higher unit-cells density and smaller angular sensitivity [26, 27, 45]. An important design challenge in frequency-selective metasurfaces is the ability to obtain specific high-order frequency responses using their strongly inter-coupled subwavelength resonances, attempted usually through multilayer FSSs. Most previous efforts have been based on effective-circuit models [26–31]. The basic FSS building blocks are metallic patches with gaps (effective capacitors C) and apertures/loops (effective inductors L) that can be combined to make effective LC resonators. Then, the shape, size and arrangement of patches and apertures in the FSS dielectric and metallic sheets are designed to accom-

plish the necessary circuit topology and element-values for the transmission desired. While such circuit models can give a good physical intuition about the expected response of a FSS, they are too approximate and less flexible for a precise design method (as explained above). This is why, although particular attention has been given to the design of elliptic filters, most of previous efforts have only achieved an approximate “quasi-elliptic” response [21–25]. In Sec. IV, we discuss the relation between QNMT and effective-circuit models to motivate appropriate structural-topology choices for different filters and scattering-zero placements. However, following our systematic filter-design procedure, we then implement microwave metasurfaces that exhibit, for a normally incident plane wave, transmission spectra matching ISF responses of various orders, bandwidths and types. Notably, we demonstrate second- and third-order elliptic filters for both bandpass and bandstop behaviors. We show that, in some cases, even though symmetric performance is desired, structural asymmetry should be used, while conversely, in cases where the ideal performance is antimetric, we also present approximate symmetric solutions. The designed metasurfaces are compatible with fabrication by printed-circuit board technology, and also offer potential electrical tunability.

II. S-MATRIX OF LOSSLESS RECIPROCAL 2-PORT SYSTEMS

We consider a linear time-independent reciprocal system, without material absorption or gain (although these could easily be included perturbatively [36]), coupled to radiation only via two ports. These are used as channels for an incoming excitation at frequency ω and outgoing scattered waves, described by a 2×2 scattering matrix S (Fig. 1). Here, we summarize some key properties of S and its QNMT model, derived in Ref. 36, that we will need in later sections.

To begin with, recall [36] that (i) the poles of S appear in pairs $(\omega_n, -\omega_n^*)$ due to realness [$S^*(i\omega) = S(-i\omega^*)$]; (ii) the zeros of $S_{21} = S_{12}$ can only appear as complex quadruplets $(\omega_o, \omega_o^*, -\omega_o, -\omega_o^*)$, real or imaginary pairs $(\omega_o, -\omega_o)$, or at $\omega_o = 0$; and (iii), for each zero-pair $(\omega_o, -\omega_o^*)$ of S_{11} , $(-\omega_o, \omega_o^*)$ is a zero-pair of S_{22} . These restrictions imply that S_{pq} is a rational function of $i\omega$ with real coefficients and, in particular, that the numerator of S_{21} is a polynomial of ω^2 with real coefficients, optionally with multiplicative $i\omega$ factors.

The system poles correspond to resonant QNMs, which can be obtained using a numerical eigensolver. The high- Q modes have frequencies ω_n and coupling coefficients to the ports $p = 1, 2$ equal to D_{pn} , which can be computed as an overlap surface integral between the n -QNM field and the p -port mode at the boundary of the scatterer, as explained in detail in Ref. 36. Their ratios $\sigma_n = D_{2n}/D_{1n}$ do not depend on the normalization of the QNMs. Moreover, any system low- Q resonances ω_n^C can admit a sim-

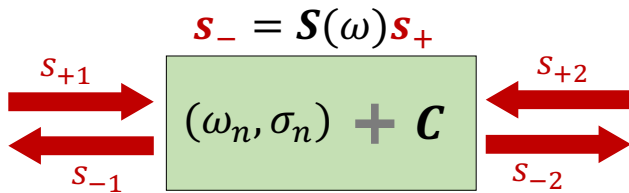


FIG. 1. A lossless reciprocal 2-port scattering system excited at frequency ω , with input and output amplitudes respectively $s_{\pm p}$, related by the S -matrix through $s_- = Ss_+$. The system supports high- Q quasi-normal modes (QNMs) with frequencies ω_n and port-coupling ratios σ_n , while low- Q resonances create an effective background response C .

plified description in terms of an effective “background” response between the two ports, quantified by a background scattering matrix C [36]. When these background QNMs have $Q \rightarrow 0$, they give a frequency-independent unitary symmetric C . In this case, our formulation from Ref. 36 shows that, when the ports are referenced at the boundary of the scatterer, enforcing energy conservation (unitary S) gives:

$$\begin{aligned}
 S &= \bar{S}C \\
 \bar{S} &= I + \sum_{n=1}^N \frac{\bar{S}^{(n)}}{i\omega - i\omega_n} \\
 \bar{S}_{pq}^{(n)} &= \sigma_{pn} \sum_{l=1}^N M_{nl}^{-1} \sigma_{ql}^* \\
 M_{nl} &= \frac{1 + \sigma_l \sigma_n^*}{i\omega_l - i\omega_n^*}, \quad \sigma_{1n} = 1, \quad \sigma_{2n} = \sigma_n,
 \end{aligned} \tag{1}$$

where σ_n are further fine-tuned from the computed values in order to satisfy also reciprocity (symmetric S via $[\bar{S}^{(n)}C]_{21} = [\bar{S}^{(n)}C]_{12}$), using a simple constrained optimization. C itself can be computed as $C = -\bar{S}_{\{\omega_n\}}$. In practice, the background Q s are small but nonzero, so C is slowly varying but not constant; nevertheless, Eq. (1) provides a good approximation for S . The distinction between high- and low- Q modes is, in fact, somewhat arbitrary and based mainly on computational convenience. In the limit where one includes all modes in \bar{S} , then $C = -I$.

\bar{S} in Eq. (1) is *uniquely* determined by the values $\{\omega_n, \sigma_n\}$ and can be easily shown [36] to satisfy, for $\gamma = \pm 1$ (extended to complex γ in Sec. III),

$$\begin{aligned}
 \bar{S}_{11\{\omega_n, \gamma\sigma_n\}} &= \bar{S}_{11\{\omega_n, \sigma_n\}}, \quad \bar{S}_{12\{\omega_n, \gamma\sigma_n\}} = \gamma^* \bar{S}_{12\{\omega_n, \sigma_n\}} \\
 \bar{S}_{21\{\omega_n, \gamma\sigma_n\}} &= \gamma \bar{S}_{21\{\omega_n, \sigma_n\}}, \quad \bar{S}_{22\{\omega_n, \gamma\sigma_n\}} = \bar{S}_{22\{\omega_n, \sigma_n\}}.
 \end{aligned} \tag{2}$$

and, by swapping ports $1 \leftrightarrow 2$,

$$\bar{S}_{11\{\omega_n, \sigma_n\}} = \bar{S}_{22\{\omega_n, 1/\sigma_n\}}, \quad \bar{S}_{21\{\omega_n, \sigma_n\}} = \bar{S}_{12\{\omega_n, 1/\sigma_n\}}. \tag{3}$$

III. FILTER DESIGN

Our goal is to design physical 2-port systems with standard network-synthesis filter responses, specifically N th-order band-pass and band-stop filters of a finite bandwidth, which are given as rational functions of frequency $H(\omega)$ with specified $2N$ complex poles [appearing as N pairs $(\omega_n, -\omega_n^*)$], $2N$ zeros (abiding by the restrictions of the previous section) and an overall constant. Attempting this design by optimizing over structural parameters to find a scattering-matrix that matches specific values of the desired $H(\omega)$ at a finite set of key frequencies can be very difficult in practice, as this highly-resonant problem can present a vast number of local extrema and lead to “stiff” constraints [41]. Instead, the eigenmode-solver-derived components of a QNMT expansion have a much slower dependence on the physical structural parameters, so they yield a more tractable optimization formulation.

It is obvious that the complex resonant frequencies ω_n of the physical system must match the complex poles of the desired filter. In this work, we show how to also enforce the desired zeros in the system response, by deriving the corresponding σ_n coefficients and the matrix C . Specifically, $|C_{21}|$ must match the desired filter background transmission and then, for exact ISFs, we find that the ratios of couplings of the QNMs’ fields to the two ports must be $\sigma_n = \pm 1$ for N odd or $\sigma_n = \pm i$ for N even, with alternating signs for consecutive modes. Enforcing $|C_{21}|$ and the N complex ω_n, σ_n results in a minimal set of $4N + 1$ real equations. We also explain that good approximate solutions can be obtained, if an overall common phase for all σ_n is allowed, according to Eqs. (10–13).

Symmetric and antimetric filters— We explained that, for a general lossless reciprocal 2-port system, the zeros of S_{11} and S_{22} are conjugates of each other, but they do not necessarily coincide. In this article, we are interested in the special cases of filters where they do coincide, so that these zeros can only appear as complex quadruplets $(\omega_o, \omega_o^*, -\omega_o, -\omega_o^*)$, real or imaginary pairs $(\omega_o, -\omega_o)$, or at $\omega_o = 0$. Their numerator is then also (as is always true for S_{21}) a polynomial of ω^2 with real coefficients, optionally with multiplicative $i\omega$ factors. These cases include, in particular, common practical amplitude filters, for which all zeros of reflection (S_{11} and S_{22}), corresponding to full transmission, lie on the real frequency axis or at infinity. To satisfy realness, this class of filters is collectively described by the condition $S_{22} = \pm S_{11}$, namely they are either symmetric or “antimetric” [35] (note [46]). Energy conservation and reciprocity then force $\sqrt{\gamma} S_{11} S_{21}^*$ to be purely imaginary for $\gamma \equiv S_{22}/S_{11} = \pm 1$, corresponding to (+) odd or (-) even number of $i\omega$ factors in the numerator of S_{11} or S_{21} .

The most important subclass comprises the ideal standard filter (ISF) approximations [1]: Butterworth (flat passband and stopband), Chebyshev (equiripple passband, flat stopband), inverse Chebyshev (equiripple stop-

band, flat passband) and elliptic (equiripple passband and stopband) (see Fig. 4). For a N^{th} -order Butterworth or Chebyshev transmission bandpass filter, S_{21} has N zeros at $\omega = 0$ (N $i\omega$ -factors in numerator) and N zeros at $\omega \rightarrow \infty$ ($2N$ zeros total). For N^{th} -order inverse Chebyshev or elliptic filters, which have zeros at finite real frequencies, S_{21} still has one zero at $\omega = 0$ and one at $\omega \rightarrow \infty$ for N odd, while all $2N$ zeros are finite for N even (no $i\omega$ factors). For a transmission bandstop filter, the same observations hold instead for S_{11} . In all ISF cases, we conclude that $S_{11}S_{21}^*$ is purely imaginary ($\gamma = 1$), if N is odd, and purely real ($\gamma = -1$), if N is even.

Conditions on C and σ_n — A partial-fraction expansion of the desired network-synthesis expresses $H(\omega)$ in terms of the complex poles, their residues, and a direct term t (which gives the limiting response at high frequencies according to the filter's type). Using the $S = \bar{S}C$ formulation of Eq. (1) for an actual physical system, we assume that C can be designed as approximately constant over the finite bandwidth of interest, where it can generally be complex. Far from the high- Q resonances ($\omega \gg |\omega_n|$), Eq. (1) dictates $\bar{S} \rightarrow I$ and thus $S \rightarrow C$. Therefore, for a transmission filter, one must design $|C_{21}| = t$. This provides design intuition for the topology of the structure, where appropriate low- Q modes are utilized to get the desired C , as we will see in practical examples later. During structural optimization, it may be difficult to find the low- Q modes contributing to C , in which case it can also be calculated efficiently as $C = \bar{S}^{-1}S$, where S is obtained via direct simulation of the structure (with the ports referenced at the scatterer boundary) and the filter-relevant high- Q modes are used to get a QNMT evaluation of \bar{S} .

For the class of filters of interest with $S_{22} = \gamma S_{11}$ ($\gamma = \pm 1$), $S \rightarrow C$ means that the unitary symmetric C also satisfies $C_{22} = \gamma C_{11}$ and that $\sqrt{\gamma}C_{11}C_{21}^*$ is purely imaginary. Now, since $\bar{S} = SC^{-1}$, we can write:

$$\bar{S} = \frac{1}{|C|} \begin{pmatrix} S_{11}\gamma C_{11} - S_{21}C_{21} & -S_{11}C_{21} + S_{21}C_{11} \\ S_{21}\gamma C_{11} - \gamma S_{11}C_{21} & -S_{21}C_{21} + \gamma S_{11}C_{11} \end{pmatrix} \quad (4)$$

so that $\bar{S}_{11} = \bar{S}_{22}$ and $\bar{S}_{21} = \gamma \bar{S}_{12}$. Further, using Eqs. (2, 3) for the dependence of \bar{S} on σ_n :

$$\begin{aligned} \bar{S}_{11\{\omega_n, \frac{1}{\sigma_n}\}} &= \bar{S}_{22\{\omega_n, \sigma_n\}} = \bar{S}_{11\{\omega_n, \sigma_n\}} = \bar{S}_{11\{\omega_n, \frac{\sigma_n}{\gamma}\}} \\ \bar{S}_{21\{\omega_n, \frac{1}{\sigma_n}\}} &= \bar{S}_{12\{\omega_n, \sigma_n\}} = \frac{1}{\gamma} \bar{S}_{21\{\omega_n, \sigma_n\}} = \bar{S}_{21\{\omega_n, \frac{\sigma_n}{\gamma}\}}. \end{aligned} \quad (5)$$

The same result applies to \bar{S}_{22} and \bar{S}_{21} , so we obtain $\bar{S}_{\{\omega_n, 1/\sigma_n\}} = \bar{S}_{\{\omega_n, \sigma_n/\gamma\}}$. From the uniqueness property mentioned earlier, we conclude that $1/\sigma_n = \sigma_n/\gamma$. Therefore, for a lossless reciprocal 2-port system:

$$S_{22} = \gamma S_{11} \Leftrightarrow \sigma_n = \pm\sqrt{\gamma}, \quad (6)$$

so that all modes have $\sigma_n = \pm 1$ for a symmetric filter ($\gamma = 1$), while $\sigma_n = \pm i$ for an antimetric ($\gamma = -1$).

(This generalizes the well-known CMT result for a single resonance, where transmission reaches 1 only for equal decay rates into the two ports [47].) Moreover, with this σ_n choice, $i\sigma_n C_{11}C_{21}^*$ is purely real.

In the particular case of ISFs, C is constant over all frequencies, so it must be real, to satisfy the realness condition. Consistently with $i\sigma_n C_{11}C_{21}^*$ real, odd-order ISFs have $\sigma_n = \pm 1$ and $C_{11}C_{21} = 0$, while $\sigma_n = \pm i$ for even order.

As detailed in Appendix A, Eq. (6) can be also derived using general arguments based on the transfer matrix. However, the scattering-matrix QNMT we used here further helps specify the choice of σ -signs to enforce the desired positions of S -coefficients zeros, as we show in the remainder of this section.

Types of Filters— For each mode n , the appropriate choice of sign for σ_n in Eq. (6) depends on the specific filter type that is being designed. We find the adequate choice analytically in the limit of large Q s, or more specifically when $\Gamma_{n,l} \ll |\Omega_n - \Omega_l|$ for $\omega_n = \Omega_n - i\Gamma_n$. Under such condition, the matrix M is dominated by its diagonal terms $M_{nn} = (1 + |\sigma_n|^2)/2\Gamma_n$, so Eq. (1) becomes:

$$\bar{S}_{pq} \approx \delta_{pq} + \sum_n \frac{\Gamma_n}{i(\omega - \Omega_n) - \Gamma_n} \frac{2\sigma_{pn}\sigma_{qn}^*}{1 + |\sigma_n|^2}, \quad (7)$$

with $\sigma_{1n} = 1$, $\sigma_{2n} = \sigma_n$. Then, away from the resonances ($\Gamma_n \ll |\omega - \Omega_n|$) and to lowest order in Γ_n , further using $|\sigma_n| = 1$ from Eq. (6), transmission is

$$S_{21} \approx C_{21} - i \sum_n \frac{\Gamma_n}{\omega - \Omega_n} (\sigma_n C_{11} + C_{21}). \quad (8)$$

As the overall background transmission $C_{21} \approx S_{21}(\omega \gg \Omega_n)$ determines the filter type, we will study its different cases separately.

Case (a) $C_{21} = 0 \Leftrightarrow |C_{11}| = 1$: This is a band-pass filter with zero transmission at $\omega \rightarrow \infty$. From Eq. (8), we have $S_{21} \propto \sum_n \Gamma_n \sigma_n / (\omega - \Omega_n)$, which, under condition Eq. (6), is proportional to a real function that can be easily used to determine the placement of its zeros. As an example, we look at the simple scenario of two modes with $\Omega_1 < \Omega_2$ and calculate the zero at

$$\omega_o \approx \frac{\Omega_2 \Gamma_1 \sigma_1 + \Omega_1 \Gamma_2 \sigma_2}{\Gamma_1 \sigma_1 + \Gamma_2 \sigma_2}. \quad (9)$$

One can easily confirm that, when $\sigma_1 = \sigma_2$, the zero appears between the modes ($\Omega_1 < \omega_o < \Omega_2$), a feature often observed in interference phenomena, such as electromagnetically induced transparency (EIT) [37, 48]. When $\sigma_1 = -\sigma_2$, it appears on the side of the mode with the smallest loss rate ($\omega_o < \Omega_1$ if $\Gamma_1 < \Gamma_2$ and $\omega_o > \Omega_2$ if $\Gamma_2 < \Gamma_1$), while there is no zero if $\Gamma_2 = \Gamma_1$ (explaining the lack of transmission zeros predicted by traditional CMT for two equal-loss coupled resonances [34] and in

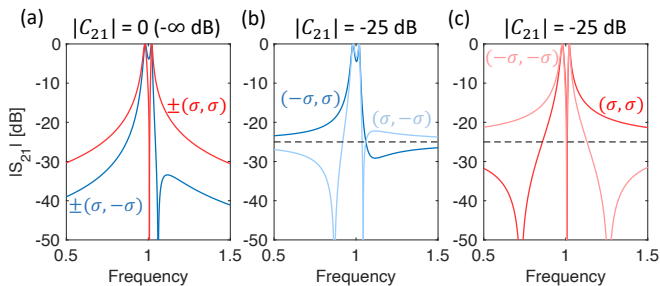


FIG. 2. Second-order filter responses, using QNM expansions of the form $S = \bar{S}C$, with two modes of frequencies $\Omega = (0.98 - 0.01i, 1.02 - 0.005i)$ and coupling ratios $(\pm\sigma, \pm\sigma)$ in \bar{S} , and with unitary reciprocal $C = \begin{pmatrix} i\sigma^*r & t \\ t & i\sigma r \end{pmatrix}$ where $r = \sqrt{1-t^2}$ and such that $\beta = i\sigma^*$ and $C_{22} = \sigma^2 C_{11}$ ($\Leftrightarrow S_{22} = \sigma^2 S_{11}$), for different values of real background transmission t indicated in the plots. We use the RWA of ignoring negative-frequency poles, so the amplitudes of S -matrix coefficients are exactly the same for any complex $\sigma = \sqrt{\gamma} = e^{i\varphi/2}$. A zero always occurs between modes of same coupling ratio (red), so filters with no zeros between the poles require opposite signs of the ratios (blue). Including negative-frequency poles would result to the same qualitative behavior and only slightly change the response away from the resonances.

symmetric ‘‘Fabry-Perot’’ systems where all Γ ’s are the same [32]). These points are illustrated in Figure 2(a).

These conclusions can be extended to the scenario of multiple high- Q modes: a real zero always occurs between two consecutive modes of same σ_n , there can only be an even (or zero) number of real zeros between two consecutive modes of opposite σ_n and, below the lowest mode or above the highest mode, a zero can exist only if there is at least one change in σ -sign.

For the ISFs with no transmission at infinity, such as a Butterworth, Chebyshev, odd-order inverse Chebyshev or odd-order elliptic, where the transmission zeros are always outside the passband, it is necessary to design σ_n with alternating signs, namely

$$\sigma_n = \pm\sqrt{\gamma}(1, -1, 1, -1, \dots) = \pm\sqrt{\gamma}(-1)^{n-1}. \quad (10)$$

Case (b) $0 < |C_{21}| \ll |C_{11}| < 1$: This is a band-pass filter with finite small transmission at $\omega \rightarrow \infty$. From Eq. (8), we have $S_{21} \approx C_{21} - iC_{11} \sum_n \Gamma_n \sigma_n / (\omega - \Omega_n)$. If we denote $\beta = C_{11}C_{21}^*/|C_{11}C_{21}|$, then, from the previous discussion, $i\sigma_n\beta = \pm i\sqrt{\gamma}\beta = \pm 1$. Therefore, S_{21} is proportional to a real expression whose zeros can be easily predicted, as in the previous case. In particular, a real zero always occurs between two consecutive modes of same σ_n . Moreover, there is an odd number of real zeros below the lowest mode, when $i\sigma_1\beta = -1$, and an even (or zero) number when $i\sigma_1\beta = 1$, with a similar result above the highest mode but for opposite signs of $i\sigma_N\beta$. This is simply illustrated in Figs. 2(b,c).

For ISFs ($\beta = \pm 1$), in this case inverse Chebyshev or elliptic of even order N ($\gamma = -1$), with a total of $N/2$

positive-frequency transmission zeros on each side of the passband, it is necessary to have

$$\sigma_n = \frac{1}{\beta} (-1)^{n-1} i^{N-1}; \quad \beta = \frac{C_{11}C_{21}^*}{|C_{11}C_{21}|}. \quad (11)$$

Case (c) $0 < |C_{11}| \ll |C_{21}| < 1$: This is a band-stop filter with finite small reflection at $\omega \rightarrow \infty$. Similar analysis by considering S_{11} dictates, for even-order inverse Chebyshev or elliptic ISFs,

$$\sigma_n = \frac{1}{\beta} (-1)^{n-1} i^{N+1}; \quad \beta = \frac{C_{11}C_{21}^*}{|C_{11}C_{21}|}. \quad (12)$$

Case (d) $C_{11} = 0 \Leftrightarrow |C_{21}| = 1$: This is a band-stop filter with zero reflection at $\omega \rightarrow \infty$ and a ISF implementation requires again simply

$$\sigma_n = \pm\sqrt{\gamma}(-1)^{n-1}. \quad (13)$$

By designing σ_n to satisfy the appropriate condition from Eqs. (10–13) according to the filter type, the pole residues in the partial-fraction expansion of $H(\omega)$ are also matched and thus the filter design is complete.

Approximate solutions— Negative-frequency modes are necessary to exactly satisfy realness. However, for filters with high- Q modes, the response can be well approximated (at positive frequencies ω) by the well-known rotating-wave approximation (RWA) of including only positive-frequency modes in QNMT. In this case, the previous results hold for any complex phase factor $\gamma = e^{i\varphi}$. Therefore, in filter design, Eqs. (10–13) permit σ_n to be tuned to the desired values up to an overall common phase factor (expressed via γ or $\beta = \pm i/\sqrt{\gamma}$). Then, the resulting filters, even after including also negative modes with their corresponding σ_n^* to satisfy realness, will be good approximations of ISFs within the bandwidth of interest.

As seen from Eq. (3), for $\sigma = \pm 1$ ($\gamma = 1$), \bar{S} is symmetric, so $S = \bar{S}C$ is also symmetric if $C_{22} = C_{11}$. Similarly, for $\sigma = \pm i$ ($\gamma = -1$), S is symmetric with $C_{22} = -C_{11}$. However, when γ is complex, reciprocity and realness of $S = \bar{S}C$ cannot be satisfied with a constant C . Since an actual physical system is obviously reciprocal, even when designed for complex γ , this means that C is necessarily non-constant, but rather slowly varying due to other modes, in a way that guarantees reciprocity. In other words, it is not possible to obtain high- Q modes verifying Eq. (6) with complex γ without additional modes proximal enough to form a frequency-dependent C .

Geometrical symmetry— $\sigma_n = \pm 1$ means that the radiative part of the modes is even or odd, which can be easily obtained using a structure with geometrical (e.g. mirror) symmetry between the two ports [47]. This can explain the increase in transmission previously observed in symmetric structures [49]. However, we will later see filter designs where it is preferable for the structure to

not be symmetric, so the modes themselves are not even or odd, even though their radiative far fields may in fact be (satisfying $\sigma_n = \pm 1$).

On the other hand, for $\gamma \neq 1$, the mode and structure have to be asymmetric anyway. In particular, even-order antimetric ISFs ($\gamma = -1$) can be made only from asymmetric structures, as confirmed for example by their known corresponding electric-circuit topologies [1]. However, we explained that good approximate filters can be obtained with γ deviating from its optimal value by a phase factor (as long as the background C is slowly varying, in contrast to being constant for ISFs). Therefore, approximate even-order ISFs can be designed also with $\gamma = 1$. To highlight this point, we later show implementations of such filters, using *symmetric* structures.

Summary— A N -order 2-port filter, whose reflection is zero at N real frequencies, obeys $S_{22} = \gamma S_{11}$ ($\gamma = \pm 1$) and consists only of modes whose radiation couples to the two ports with the ratios $\sigma_n = \pm \sqrt{\gamma}$. To design standard filters, these ratios must alternate sign among consecutive modes, and a background scattering C , appropriate for the desired filter type, must be established [Eqs. (10–13)]. Approximate filters can also be designed with complex unitary γ . Once the QNMT design objectives (background transmission $|C_{21}|$, eigenfrequencies ω_n and port-coupling ratios σ_n) have been determined for the desired filter profile, the physical metasurface parameters can be identified using adequate optimization/nonlinear-solver tools.

IV. MICROWAVE METASURFACES

The analytical criteria we have presented in this article give a direct pathway to precisely design high-order microwave metasurface filters. In this section, we obtain all types of bandpass and bandstop ISFs with different orders and bandwidths. For each desired filter, we choose a fixed topology, based on circuit-theory principles and also on intuition from QNMT itself (for the background scattering C), with few unknown physical parameters. These are then optimally identified by simply applying a multivariable solver of nonlinear systems of equations on the filter conditions derived in section III. This rather “traditional” approach leads to very rapid computational design, as physics and analytics have already been used to facilitate the job of the optimizer.

Unless otherwise stated, in all microwave metasurfaces studied in this article: (i) We use perfect metal with thickness $18\mu\text{m}$ (corresponding to 0.5oz copper). (ii) The square-lattice period a and the centers of the crosses are the same for all patterned layers. (iii) We study for frequencies below the first diffraction cutoff ($f_{\text{cut}} = c/a$ at normal incidence), so only transmission and reflection need to be considered. (iv) There is C_{2v} symmetry, so the response for normal incidence is independent of the polarization \hat{e} and indeed only 2 ports are needed.

(v) Numerical computation of the “exact” frequency response $S(\omega)$ for plane-wave excitation as well as of the eigenmodes (ω_n, σ_n) for use in our QNMT is carried out using COMSOL Multiphysics [50], as detailed in Ref. 36. In the Supplemental Material [51], we provide tables with the calculated QNMs for every metasurface presented.

A. Second-order bandpass filter - Circuit model

We start by studying a simple *symmetric* second-order metasurface, in order to build some physical intuition on how a particular structural topology can be modeled by an effective circuit, to relate this circuit to the QNMT, and to derive design guidelines for transmission-zero placement. The metasurface, shown in Fig. 3(a), is formed by two planar metallic sheets sandwiched between three uniform dielectric layers. A square array (with period a) of narrow cross-like apertures in each metallic sheet creates a resonance, which can be modeled in the subwavelength limit ($a \ll \lambda$) as an effective shunt parallel $L_a C_a$ ($\equiv 1/\omega_a^2$) to a plane wave incoming from free space with impedance Z . The inductance L_a originates from the current flowing around the edge of the aperture, while the capacitance C_a comes from the opposite-charge accumulation across facing sides of this narrow gap [see Fig. 3(a)]. The connected topology of the metallic sheets represents a short-circuit to an incident plane wave at long wavelengths (shunt L_a), leading to no transmission at zero frequency. Moreover, a longitudinal inductance L_b couples the apertures on the two metallic sheets, corresponding both to first-order transmission-line effects of the thin dielectric layer and to the direct mutual inductance between the apertures. Finally, capacitance C_b builds up between the two metallic sheets [see Fig. 3(a)], which is an interesting feature that has an important consequence: it leads to the emergence, in series with the path of incident-wave propagation (longitudinally), of a parallel-resonant $L_b C_b$, which becomes an open circuit at the frequency $\omega_b = 1/\sqrt{L_b C_b}$, thus leading to a zero in the transmission function. The final equivalent-circuit model is given in Fig. 3(b), corresponding to a passband filter with a finite-frequency zero.

The transmission spectrum can be computed through $S_{21} = 2V_{\text{out}}/V_{\text{in}}$ [1], and with $y_j = Z(1/\omega L_j - \omega C_j)$ for $j = a, b$ we obtain:

$$S_{21}(\omega) = \frac{2iy_b}{(1 + iy_a)(1 + i(y_a + 2y_b))}. \quad (14)$$

This clearly shows transmission zeros at $\pm\omega_b$, and also at $\omega = 0$, $\omega \rightarrow \infty$ (bandpass behavior). Denoting the loss rates $\Gamma_j = 1/(2ZC_j)$, the denominator shows the system poles at $\pm\Omega_1 - i\Gamma_1$ and $\pm\Omega_2 - i\Gamma_2$, where $\Gamma_1 = \Gamma_a$, $\Omega_1 \approx \omega_a$, $\Gamma_2 = 1/(1/\Gamma_a + 2/\Gamma_b)$, $\Omega_2 \approx \Gamma_2(\omega_a/\Gamma_a + 2\omega_b/\Gamma_b)$. One system resonance is identical to the single-sheet resonance, while the second is affected also by the inter-sheet couplings: it is always narrower ($\Gamma_2 < \Gamma_1$) and $\Omega_2 \geq \Omega_1$ if $\omega_b \geq \omega_a$.

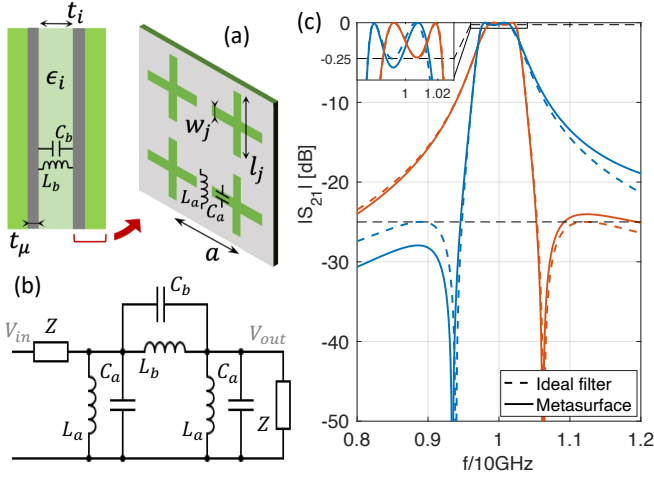


FIG. 3. (a) Symmetric metasurface for a second-order bandpass filter centered at 10 GHz with a single transmission-zero, designed for 0.25 dB passband ripple and 25 dB stopband attenuation (black dashed lines). (b) Equivalent circuit model. The coupling $L_b C_b$ gives the transmission-zero. (c) Transmission spectrum of two optimized structures with a zero respectively on the left (L) and on the right (R) of their transmission peaks. Parameters for structure (L): $a = 6\text{mm}$, $w_1/a = w_2/a = 0.0479$, $l_1/a = l_2/a = 0.846$, $t_1/a = t_3/a = 0.493$, $t_2/a = 0.257$, $\epsilon_1 = \epsilon_3 = 1.43$, $\epsilon_2 = 14.51$. Parameters for structure (R): $a = 9.34\text{mm}$, $w_1/a = w_2/a = 0.00877$, $l_1/a = l_2/a = 0.905$, $t_1/a = t_3/a = 0.0237$, $t_2/a = 0.0966$, $\epsilon_1 = \epsilon_3 = 4.12$, $\epsilon_2 = 3.80$.

When ω is close to the positive resonances, the RWA $y_j \approx (\omega_j - \omega)/\Gamma_j$ effectively drops the negative resonances. Then, a partial-fraction expansion of Eq. (14) can be obtained:

$$S_{21}(\omega) \approx \frac{i\Gamma_1}{\omega - (\Omega_1 - i\Gamma_1)} - \frac{i\Gamma_2}{\omega - (\Omega_2 - i\Gamma_2)}, \quad (15)$$

This is identical to the QNMT result in Eq. (1) with $\sigma = (-1, 1)$ and $C = I$. As mentioned earlier, the two *different* values for the decay rate Γ lead to a transmission zero, which is not usually described in typical CMT models that assume equal Γ for the two resonances.

We saw from Eq. (9) that this zero ω_b appears on the side of the resonance with the smallest loss rate, which is Γ_2 in this case, so $\omega_b < \Omega_2 < \Omega_1 = \omega_a \Leftrightarrow L_a C_a < L_b C_b$ or the opposite order. Therefore, we have a recipe to design the zero for this metasurface, based on the equivalent circuit elements. To translate those to physical structural parameters, we observe that, in the quasi-static limit, $L_b \propto t_2$ (see Appendix B) and $C_b \propto \epsilon_2/t_2$, where t_2 is the small separation between the two metallic sheets and ϵ_2 is the dielectric constant of the separating layer. This means that $L_b C_b \propto \epsilon_2$ and does not depend on t_2 to first order. On the other hand, $L_a C_a$ also does not depend on t_2 , but it has a weighted dependence on ϵ_1 and ϵ_2 . The location of the transmission zero relative to the poles then mainly depends on the ratio of permittivities of the two dielectric materials. In particular, a zero at a frequency

below the poles is obtained using a large $\epsilon_2/\epsilon_1 > 1$.

We can also use Eq. (15) to compute the full-transmission frequencies ($|S_{21}(\omega_t)| = 1$):

$$\omega_t = \frac{\Omega_1 + \Omega_2}{2} \pm \sqrt{\left(\frac{\Omega_1 - \Omega_2}{2}\right)^2 - \Gamma_1 \Gamma_2}. \quad (16)$$

We see that there are two full-transmission maxima between Ω_1 and Ω_2 , as long as the eigenfrequencies are well separated ($|\Omega_1 - \Omega_2| > 2\sqrt{\Gamma_1 \Gamma_2}$).

We can now use the QNMT to design second-order bandpass filters with a transmission-zero either on the right or on the left of the transmission peaks. In both cases, we choose the two complex eigenfrequencies, for which Eq. (15) gives a transmission peak-to-peak passband ripple of 0.25 dB, a stopband attenuation of at least 25 dB and a 3dB-bandwidth of 5% around the center frequency $f_c = \omega_c/2\pi = 10$ GHz. (For comparison, we will target these passband/stopband limits and center frequency for all filters designed in this article.) Then, we use the multivariable nonlinear-equation solver to find the structural parameters that will make the eigenmodes of the metasurface of Fig. 3(a) match those desired eigenfrequencies and with port-coupling ratios $\sigma = \pm(1, -1)$. Results for optimized structures are shown in Fig. 3(c). We note that, as expected, the structure with a transmission-zero at smaller frequencies has a larger dielectric constant for the inside layer. We also see that the shapes of the transmission spectra deviate somewhat from the ideal filters. This is mainly due to higher-frequency resonances that affect the scattering matrix (acting as a background C) and make it different from the two-poles approximation of Eq. (15), leading to slight reduction of transmission at low frequencies and increase at higher ones. As commonly known for metasurfaces, higher-order diffraction modes can be pushed away by looking, if possible, for solutions with reduced periodicity a and higher permittivities ϵ_j .

B. Third-order bandpass filters

Using the QNMT design method, as well as guidance from the previous two-pole bandpass structure, we now design all four standard types mentioned in section III for third-order bandpass filters. The three poles necessary for each wanted filter are given by standard analytical expressions or software tools [1]. Since all filter types are of third order with $C_{21} = 0$ [case (a)], we see from Eq. (10) that we trivially need port-coupling coefficients with ratios $\sigma \propto (1, -1, 1)$ for the three modes.

To implement these filters, we use a structure with the same unit-cell topology as in Fig. 3(a), but with three metallic sheets and four dielectric layers. Based on the insight gained in section IV A from the effective circuit model, we realize that each of the inside layers will create a longitudinal parallel $L_j C_j \propto \epsilon_j$ resonance, which will cause a transmission zero $\propto 1/\sqrt{\epsilon_j}$. For the inverse

Chebyshev and elliptic filters, two *distinct* zeros are required. Therefore, we need different dielectric constants ϵ_j for the inside layers. This means that the physical structure for these filter types must *not* be symmetric, so their modes are not even or odd, even if their radiative tails are $[\sigma = (1, -1, 1)]$. On the other hand, Butterworth and Chebyshev filters do not have real zeros, so there we can choose a symmetric structure, which simplifies the optimization problem, as only eigenfrequencies need to be matched (in the correct order of modal symmetry). However, for these “zeroless” ISFs, the challenge with the chosen metasurface topology is to push away from our bandwidth the unavoidable zero that will arise from the inside layers. The simplest way to accomplish this, is to look for solutions where these layers are thick enough that the second-order dependence of the longitudinal parallel $L_j C_j$ on t_j moves the zero to sufficiently high frequencies. Different topologies could also be devised that eliminate either the mutual inductance or capacitance between sheets.

Again by optimizing the structural topology, for each filter, we get the desired three complex resonant frequencies ω_n and their corresponding σ_n . Transmissions of the optimized metasurfaces that implement the four filter types with $\sim 5\text{-}6\%$ 3dB-bandwidth are shown in Fig. 4(a), while in Fig. 4(b) only for elliptic filters with varying bandwidth ($\sim 2\text{-}10\%$). We note a good agreement with the ideal filters, except for small discrepancies again due to effects from higher-order modes and to small errors in the values of optimized resonances. Notice that, indeed, Butterworth and Chebyshev filters require thick inside dielectric layers to move the zero away and that smaller bandwidths need higher ϵ_j to increase the modal Q s. Moreover, we test the effect of metal (here, copper) losses on an elliptic filter and find that it mainly just reduces the values of the transmission peaks (only by ~ 0.5 dB at 10 GHz operation).

C. Third-order elliptic bandstop filter

In order to design a third-order *bandstop* filter, we now need to achieve a full-transmission background $|C_{21}| = 1$ [case (d)], and then Eq. (13) dictates again three QNMs with $\sigma \propto (1, -1, 1)$. As reviewed in section II, the background- C design can generally be understood using the system low- Q modes and, in particular, a fully-transmissive C can be achieved by a mode with infinite radiative rate, which effectively models free space [36]. Thus, as expected, we need a physical structure with a very small effective index (~ 1), while still able to support the required high- Q resonances. Moreover, since we want full transmission at zero frequency, the metallic components now should not have a fully-connected topology. Therefore, relying on the principle of duality, we choose, in place of each metallic sheet with cross apertures, an array of non-connected thin metallic crosses. These are supported by dielectric crosses,

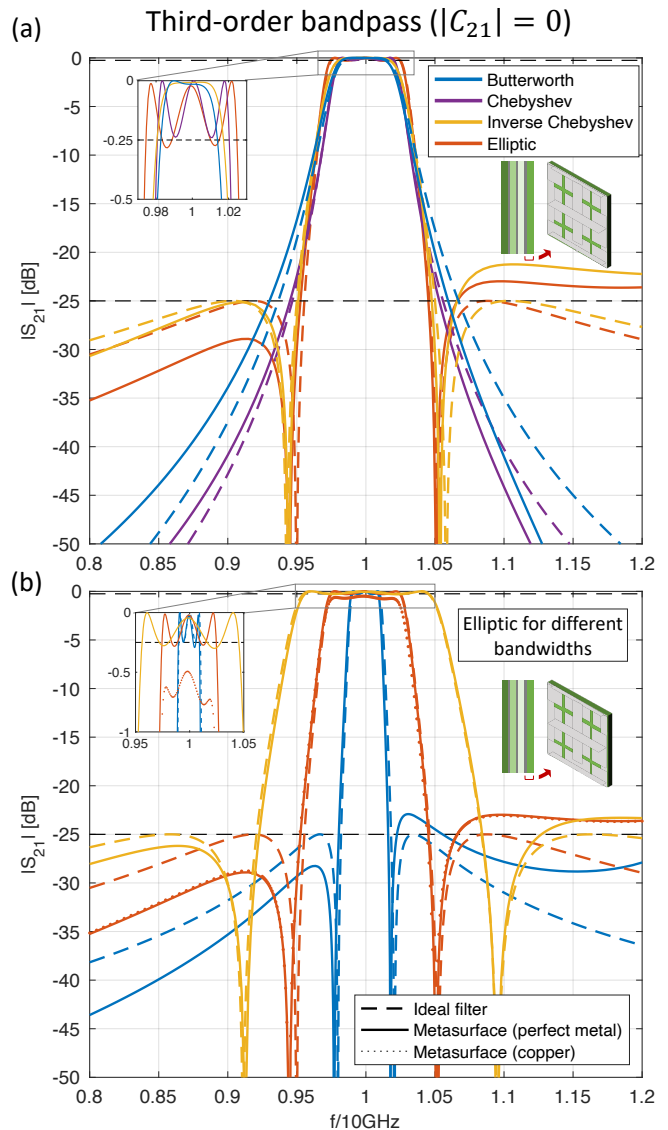


FIG. 4. Optimized third-order bandpass filters (a) of different types with same bandwidth and (b) elliptic only for different bandwidths. We use the same structure as in Fig. 3 but with three metallic sheets and four dielectric layers. Physical parameters are provided in Appendix C. We notice good agreement of lossless structures (solid lines) with ideal filters (dashed lines), except for small deviations mainly due to effects from high-order modes. Copper losses (dotted line) reduce peak transmission while preserving the filter’s shape.

also non-connected to minimize the total effective index. The structure is shown as an inset in Fig. 5(a). Its effective circuit model now sees each array of crosses as a shunt series- LC resonance, where L is the inductance of the cross wires and C is the capacitance across adjacent crosses within each array [see Fig. 5(a)], and then the couplings between arrays are effectively longitudinal parallel- LC , where C is the capacitance across facing (co-centric) crosses and L is the first-order transmission-line model of propagation through the free space, but also

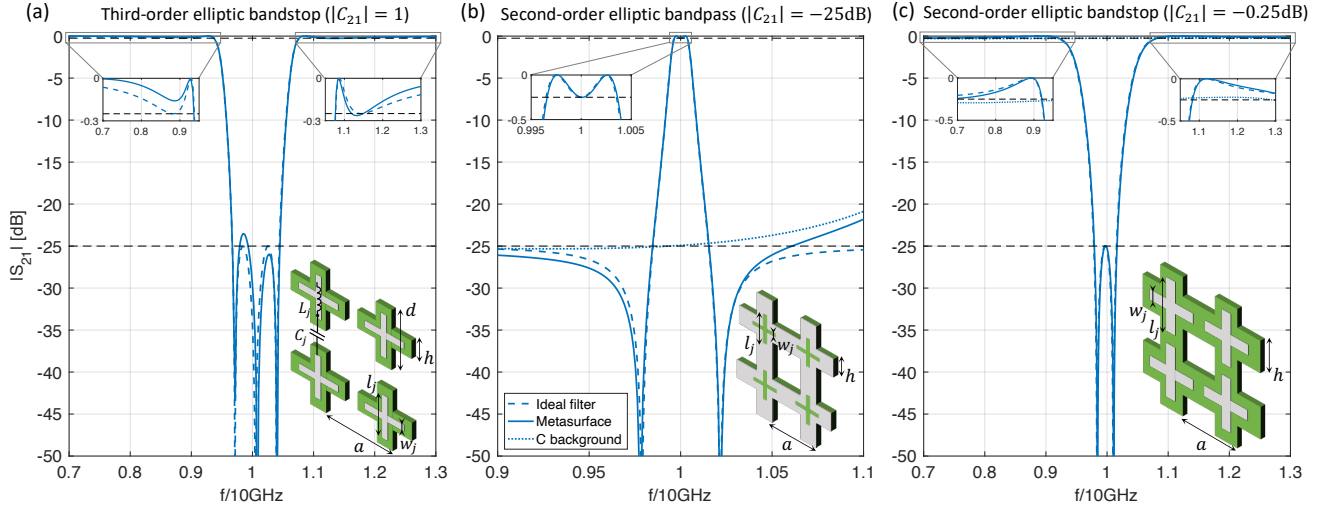


FIG. 5. (a) Third-order elliptic bandstop filter. The structure has three metallic-cross arrays and four dielectric layers with parameters: $a = 16.99\text{mm}$, $h/a = 0.03$, $d/a = 0.619$, $w/a = (1.53, 3.73, 1.61) \times 10^{-3}$, $l/a = (0.558, 0.589, 0.524)$, $t/a = (0.166, 0.358, 0.441, 0.183)$, $\epsilon = (4.76, 3.22, 4.05, 4.50)$. (b) Second-order elliptic bandpass filter. The structure has two metallic sheets and three dielectric layers with parameters: $a = 17.571\text{mm}$, $h/a = 0.456$, $w_1/a = w_2/a = 6.08 \times 10^{-3}$, $l_1/a = l_2/a = 0.4355$, $t_1/a = t_3/a = 0.3072$, $t_2/a = 0.3169$, $\epsilon_1 = \epsilon_3 = 3.82$, $\epsilon_2 = 1.893$. (c) Second-order elliptic bandstop filter. The structure has two metallic-cross arrays and three dielectric layers with parameters: $a = 18.70\text{mm}$, $h/a = 0.181$, $w_1/a = w_2/a = 2.74 \times 10^{-3}$, $l_1/a = l_2/a = 0.514$, $t_1/a = t_3/a = 0.204$, $t_2/a = 0.332$, $\epsilon_1 = \epsilon_3 = 1.60$, $\epsilon_2 = 3.10$. All filters satisfy quite well the marked requirements (black dashed lines) and agree with the ideal filters.

includes the small contribution (a large in-parallel value, see Appendix B) of the mutual inductance between facing crosses. This circuit can implement the desired ISF, where each shunt series- LC or longitudinal parallel- LC can directly impose one of the required three distinct transmission zeros.

An example of an optimized structure with a third-order elliptic bandstop response of 12% 3dB-bandwidth is shown in Fig. 5(a). We note again the very good agreement compared to the ideal filter. Notice that, in duality to the passband filter, the permittivity of one inside dielectric turns out to be *smaller* than the outside layers.

D. Second-order elliptic bandpass and bandstop filters

To complete our set of design examples, we now demonstrate second-order elliptic bandpass and bandstop metasurface filters. In this case, we need to design a specific non-trivial background C , in particular, C_{21} must be roughly constant within the bandwidth of interest and its amplitude set respectively to the desired stopband minimum attenuation value (-25 dB) [case (b)] or passband maximum ripple value (-0.25 dB) [case (c)]. Furthermore, the coefficients σ_n should respectively satisfy Eq. (11) or Eq. (12). As discussed in section III, for even-order ISFs, $\gamma = -1$ and C is a real constant matrix, so $\beta \equiv C_{11}C_{21}^*/|C_{11}C_{21}| = \pm 1$ and $\sigma_n = \pm i$, which corresponds to asymmetric structures, such as the standard circuit topologies of even-order ISFs. However, we ex-

plained that approximate solutions with a different unitary γ are possible (using the RWA) and here we present *symmetric* structures ($\gamma = 1$) exhibiting a second-order elliptic filter response within the bandwidth of interest. Since symmetry guarantees $\sigma_n = \pm 1$, Eqs. (11,12) become design objectives for β , which must respectively match $\pm i/\sigma_1$.

For the bandpass filter (with two transmission zeros), we use as starting point for the structural topology that from Fig. 3(a) corresponding to a second-order bandpass filter with only one zero. There, the large metallic sheets led to $C_{21} = 0$. In order to increase $|C_{21}|$ to the small required -25 dB around the filter center-frequency ω_c , we open holes through the entire metasurface, as shown in Fig. 5(b), so that some of the incident wave will directly go through without coupling to the high- Q resonances of the crosses. Excluding those two high- Q modes, using QNMT we calculate $C = \tilde{S}_{\{\omega_c\}}$, and it turns out that even-odd pairs of *almost* degenerate low- Q modes below ω_c together with higher-order modes lead to a background with a flat small $|C_{21}|$ and constant β over a fairly large frequency range (see modes in Supplemental Material [51]). [Traditionally, one would approximate C by simulating an effective background structure (e.g. where the cross apertures which cause the high- Q resonances are closed), but the result is inaccurate (-19 dB instead of -25 dB).] The optimization then consists of enforcing the values of the two complex eigenfrequencies, $|C_{21}(\omega_c)| = -25$ dB and, from Eq. (11), $\beta(\omega_c) = i/\sigma_1$. The transmission of the designed structure is shown in Fig. 5(b) and agrees very well with the 1%-bandwidth

ISF spectrum. It turns out that the modal symmetry is $\sigma = (-1, 1)$, so $\beta(\omega_c) = -i$. Note that, since each metallic sheet is still connected (in a topological sense), the transmission at very long wavelengths will still go to zero.

For the second-order bandstop elliptic filter, we use as starting point the structural topology from Fig. 5(a) for the third-order bandstop filter, but with two metallic-cross arrays sandwiched between three dielectric layers. There, the effective refractive index of the entire metasurface was designed small to get $|C_{21}(\omega_c)| \approx 1$. In order to decrease $|C_{21}|$ to the required -0.25 dB, we connect the dielectric crosses, as shown in Fig. 5(c), to reflect back some of the incident wave. In QNMT terms, an averaging over the metasurface leads to an effective slab of low refractive index, which supports equispaced ‘‘Fabry-Perot’’ low- Q modes $\omega_n^C = n\Omega^C - i\Gamma^C$ [32]; the ‘‘Fabry-Perot’’ transmission hits $|C_{21}| = 1$ at Ω_n^C , but is less than 1 and flat between modes $[n\Omega^C, (n+1)\Omega^C]$, with roughly constant $\beta \approx i$ if n even (and $\beta \approx -i$ if n odd). For this structure, it turns out that these modes ω_n^C have such a small Q (see modes in Supplemental Material [51]) that it is difficult to accurately find all of those contributing to $C(\omega_c)$. Therefore, we instead calculate it indirectly from $C(\omega_c) = \bar{S}^{-1}(\omega_c)S(\omega_c)$, as explained earlier. [Again, the traditional method of an effective background structure (removing the metallic crosses) gives a noticeably less accurate estimate of C (-0.11 dB instead of -0.25 dB).] The two high- Q modes have symmetry $\sigma = (-1, 1)$, consistent with $\beta(\omega_c) = i$ from Eq. (12), and the optimized final structure has transmission shown in Fig. 5(c), matching precisely an elliptic bandstop ISF of 10% bandwidth.

E. Fabrication and tunability

All the metasurface filters that we presented were based on a layered topology with metallic sheets sandwiched between dielectric layers. This layered form was chosen, because it has the great advantage of allowing easy fabrication. Especially in the cases where patterning is only on the metallic sheets, these metasurfaces can be manufactured even with widespread printed-circuit board (pcb) techniques. In fact, all designed ISFs presented in this article used dielectrics with permittivities less than 11.2, which is roughly the upper limit for (typically Al_2O_3 -based) low-loss materials compatible with pcbs. Furthermore, the clear separation between metallic sheets allows them to be connected to separate electrodes, where voltage can be applied to potentially tune the permittivity of the intermediate dielectrics, if those are chosen to be tunable materials (liquid crystals, ferroelectrics etc.) [52]. Previous attempts at elliptic filters have usually employed topologies with shunt metal paths connecting different metal sections within the metasurface, which hinders both these benefits [22–24].

V. CONCLUSIONS

We have presented a systematic method using eigen-solvers for designing standard filters or other useful transmission/reflection spectra, especially ones with multiple finite real zeros, allowing ultra-compact devices with spatially overlapping resonances (unlike previous circuit-theory or CMT approaches). It is based on a non-normalized QNM expansion of the system scattering matrix S and entails identifying the necessary background response C , the exact complex eigenfrequencies ω_n of these modes, and the values of the ratios σ_n with which these modes must couple to the system coupling ports, to achieve the desired scattering frequency profile. An efficient optimization procedure is then applied to determine the structural parameters (geometry and materials) that meet these criteria. We have demonstrated the method for microwave planar metasurface filters, for all standard amplitude-filter types (especially the most challenging, elliptic), for both bandpass and bandstop behaviors, and for a variety of frequency bandwidths.

In our examples, we used fixed topologies, guided by general physical intuition from circuit models, and then applied a simple multi-variable equation solver to obtain a small set of structural parameters. In principle, our conditions can also be combined with various large-scale topology-optimization algorithms (where every ‘‘point’’ in space is a degree of freedom) and solver methods [39]. While we focused on amplitude standard filters, our design process can be used for any desired scattering spectrum, by fitting it to QNMT to extract the corresponding eigenmode optimization objectives (ω_n, σ_n) . Moreover, it should be clear that the accurate QNMT prediction of the time delay [36] also makes the theory applicable to design phase filters, such as all-pass delay filters [53] (useful also for metalenses [54]). Our design method was demonstrated for microwave metasurfaces, but it can also be used for resonant systems with any qualitatively similar physics, such as mechanical, acoustic, photonic, or quantum-electronic filters.

ACKNOWLEDGMENTS

This work was supported in part by the U.S. Army Research Office through the Institute for Soldier Nanotechnologies at MIT under award W911NF-18-2-0048, by the Simons Foundation collaboration on Extreme Wave Phenomena, and by Lockheed Martin Corporation under award RPP2016-005.

Appendix A: Transfer-matrix formalism

For a 2-ports system as in Fig. 1, the (forward) transfer matrix is defined as:

$$\begin{pmatrix} s_{+1} \\ s_{-1} \end{pmatrix} = \begin{pmatrix} T_{11} & T_{12} \\ T_{21} & T_{22} \end{pmatrix} \begin{pmatrix} s_{-2} \\ s_{+2} \end{pmatrix} \quad (\text{A1})$$

and is related to the scattering matrix via the transformation:

$$T = \frac{1}{S_{21}} \begin{pmatrix} 1 & -S_{22} \\ S_{11} & -\det(S) \end{pmatrix}. \quad (\text{A2})$$

In terms of the T matrix, on the real- ω axis, realness is expressed as $T^*(i\omega) = T(-i\omega)$ and energy conservation as $|T_{11}|^2 - |T_{21}|^2 = |T_{22}|^2 - |T_{12}|^2 = 1$, $T_{11}^*T_{12} = T_{21}^*T_{22}$, while reciprocity holds anywhere on the complex- ω plane and is written as $\det(T) = 1$.

At a system complex pole ω_n , there are non-zero outgoing fields ($s_{-1}, s_{-2} \neq 0$) without an input ($s_{+1} = s_{+2} = 0$), so $T_{11}(\omega_n) = 0$. Since then $D_{1n} \propto s_{-1}$ and $D_{2n} \propto s_{-2}$, the ports-coupling ratio of the mode is $\sigma_n = 1/T_{21}(\omega_n)$ and reciprocity further mandates $T_{12}(\omega_n) = -1/T_{21}(\omega_n) = -\sigma_n$.

The types of filters we are interested in satisfy $S_{22} = \gamma S_{11}$, namely $T_{12} = -\gamma T_{21}$. Therefore, for reciprocal such filters, we get $\sigma_n^2 = -T_{12}(\omega_n)/T_{21}(\omega_n) = \gamma$, as in Eq. (6) of the main text. (Reminder that, if realness must hold, then $\gamma = \pm 1$.)

Inversely, consider a unitary reciprocal system where all the modes verify $\sigma_n^2 = \gamma$. We write $S_{pq}(\omega) = A_{pq}(\omega)/P(\omega)$, where $P(\omega) = \prod_n(\omega - \omega_n)$ includes all the $2N$ poles ω_n and $A_{pq}(\omega)$ is a polynomial of degree at most $2N$, so Eq. (A2) implies that $T_{12}(\omega) = -A_{22}(\omega)/A_{21}(\omega)$ and $T_{21}(\omega) = A_{11}(\omega)/A_{21}(\omega)$. At a pole, we have $T_{12}(\omega_n) = -\sigma_n^2 T_{21}(\omega_n) = -\gamma T_{21}(\omega_n)$, thus $A_{22}(\omega_n) - \gamma A_{11}(\omega_n) = 0$ [because $A_{21}(\omega_n) \neq 0$]. Since

the degree of $A_{22} - \gamma A_{11}$ is at most $2N$, we then have $A_{22}(\omega) - \gamma A_{11}(\omega) = \alpha P(\omega) \Leftrightarrow S_{22} = \gamma S_{11} + \alpha$, where α is a constant. Now, assuming a unitary system, we have $|S_{22}|^2 = |\gamma S_{11} + \alpha|^2 = |S_{11}|^2 \Leftrightarrow |\alpha|^2 + 2\text{Re}[\alpha^* \gamma S_{11}(\omega)] = 0$ at *all* real frequencies ω , leading to $\alpha = 0$ and thus $S_{22} = \gamma S_{11}$.

Appendix B: Inductive coupling between closely-spaced apertures

For two inductors L_1, L_2 with mutual inductance M , the standard T-type coupling network with elements $L_1 - M$, $L_2 - M$ and M is converted to the Π -type network, used in our circuit models, with element values $(L_1 L_2 - M^2)/(L_2 - M)$, $(L_1 L_2 - M^2)/(L_1 - M)$ and $(L_1 L_2 - M^2)/M$. The last element represents the longitudinal inductive coupling L_b in our circuits, which becomes small for large mutual inductance $M < \sqrt{L_1 L_2}$ (and vice versa).

When L_1, L_2 are aperture-type, M scales linearly with their on-axis distance t as $M \approx M_0 - \xi t$ for $\xi t \ll M_0$ [55], so $L_b \approx L_1 L_2 / M_0 - M_0 + \xi t$. When the two apertures are not too dissimilar, $M_0 \approx \sqrt{L_1 L_2}$, so we finally get $L_b \approx \xi t$ for $M_0 (L_1 L_2 / M_0^2 - 1) \ll \xi t \ll M_0$. Moreover treating the dielectric layer as a very short transmission line, its equivalent circuit model is also just an inductor with $L'_b \approx \xi' t$, where ξ' the inductance per unit length. Combining the two sources of inductance we conclude the rough scaling $L_b \propto t$.

Appendix C: Third-order bandpass filters' structural parameters

Below are the structural parameters for the third-order bandpass filters of Fig. 4:

Type	a (mm)	w_1/a	w_2/a	w_3/a	l_1/a	l_2/a	l_3/a	t_1/a	t_2/a	t_3/a	t_4/a	ϵ_1	ϵ_2	ϵ_3	ϵ_4
Butterworth	13.49	0.024	0.003	0.024	0.805	0.709	0.805	–	0.445	0.445	–	1	2.41	2.41	1
Chebyshev	12.02	0.0099	0.0027	0.0099	0.7896	0.6639	0.7896	–	0.483	0.483	–	1	3.45	3.45	1
Inverse Chebyshev	9.83	0.221	0.050	0.055	0.772	0.645	0.944	–	0.278	0.096	0.018	1	6.72	3.64	2.73
Elliptic 1	10.00	0.28	0.034	0.009	0.501	0.535	0.849	–	0.451	0.026	0.020	1	8.21	3.95	3.00
Elliptic 2	9.175	0.222	0.068	0.022	0.692	0.607	0.908	–	0.343	0.071	0.021	1	8.58	4.42	3.19
Elliptic 3	10.45	0.207	0.012	0.071	0.806	0.710	0.992	–	0.187	0.066	0.014	1	5.72	2.61	3.41

[1] H. G. Dimopoulos, *Analog Electronic Filters: Theory, Design and Synthesis* (Springer Science & Business Media, 2011).
[2] B. E. Little, S. T. Chu, H. A. Haus, J. Foresi, and J.-P. Laine, *Journal of Lightwave Technology* **15**, 998 (1997).
[3] S. Fan, P. R. Villeneuve, J. D. Joannopoulos, and H. A. Haus, *Optics Express* **3**, 4 (1998).

[4] C. Manolatu, M. Khan, S. Fan, P. R. Villeneuve, H. Haus, and J. Joannopoulos, *IEEE Journal of Quantum Electronics* **35**, 1322 (1999).
[5] M. A. Popovic, T. Barwicz, M. R. Watts, P. T. Rakich, L. Socci, E. P. Ippen, F. X. Kärtner, and H. I. Smith, *Optics Letters* **31**, 2571 (2006).
[6] S. Xiao, M. H. Khan, H. Shen, and M. Qi, *Optics Express*

- 15**, 14765 (2007).
- [7] H.-C. Liu and A. Yariv, *Optics Express* **19**, 17653 (2011).
- [8] Z. Dai, J. Wang, and Y. Heng, *Optics Express* **19**, 3667 (2011).
- [9] W. Bogaerts, P. De Heyn, T. Van Vaerenbergh, K. De Vos, S. Kumar Selvaraja, T. Claes, P. Dumon, P. Bienstman, D. Van Thourhout, and R. Baets, *Laser & Photonics Reviews* **6**, 47 (2012).
- [10] T.-K. Wu, *Frequency Selective Surface and Grid Array*, Vol. 40 (Wiley-Interscience, 1995).
- [11] J. C. Vardaxoglou, *Frequency Selective Surfaces: Analysis and Design* (Research Studies Press, 1997).
- [12] B. A. Munk, *Frequency Selective Surfaces: Theory and Design* (John Wiley & Sons, 2005).
- [13] D. Morgan, *Surface Acoustic Wave Filters: With applications to Electronic Communications and Signal Processing* (Academic Press, 2010).
- [14] A. Colombi, D. Colquitt, P. Roux, S. Guenneau, and R. V. Craster, *Scientific Reports* **6**, 1 (2016).
- [15] B. Rostami-Dogolsara, M. K. Moravvej-Farshi, and F. Nazari, *Physical Review B* **93**, 014304 (2016).
- [16] L. D'Alessandro, E. Belloni, R. Ardito, F. Braghin, and A. Corigliano, *Applied Physics Letters* **111**, 231902 (2017).
- [17] D. Colquitt, A. Colombi, R. Craster, P. Roux, and S. Guenneau, *Journal of the Mechanics and Physics of Solids* **99**, 379 (2017).
- [18] G. Manara, A. Monorchio, and R. Mittra, *Electronics Letters* **35**, 1400 (1999).
- [19] D. J. Kern, D. H. Werner, A. Monorchio, L. Lanuzza, and M. J. Wilhelm, *IEEE Transactions on Antennas and Propagation* **53**, 8 (2005).
- [20] J. A. Bossard, D. H. Werner, T. S. Mayer, J. A. Smith, Y. U. Tang, R. P. Drupp, and L. Li, *IEEE Transactions on Antennas and Propagation* **54**, 1265 (2006).
- [21] Z. H. Jiang, S. Yun, L. Lin, J. A. Bossard, D. H. Werner, and T. S. Mayer, *Scientific Reports* **3**, 1 (2013).
- [22] G. Q. Luo, W. Hong, Q. H. Lai, K. Wu, and L. L. Sun, *IEEE Transactions on Microwave Theory and Techniques* **55**, 2481 (2007).
- [23] B. Li and Z. Shen, *IEEE Transactions on Antennas and Propagation* **61**, 3053 (2013).
- [24] Q. Lv, C. Jin, B. Zhang, and R. Mittra, *IEEE Access* **7**, 55833 (2019).
- [25] R.-X. Liao, S.-W. Wong, Y. Li, J.-Y. Lin, B.-Y. Liu, F.-C. Chen, and Z. Quan, *IEEE Access* **8**, 113675 (2020).
- [26] K. Sarabandi and N. Behdad, *IEEE Transactions on Antennas and Propagation* **55**, 1239 (2007).
- [27] F. Bayatpur and K. Sarabandi, *IEEE Transactions on Microwave Theory and Techniques* **56**, 774 (2008).
- [28] O. Luukkonen, C. Simovski, G. Granet, G. Goussetis, D. Lioubtchenko, A. V. Raisanen, and S. A. Tretyakov, *IEEE Transactions on Antennas and Propagation* **56**, 1624 (2008).
- [29] F. Bayatpur, *Metamaterial-Inspired Frequency-Selective Surfaces.*, Ph.D. thesis (2009).
- [30] F. Mesa, R. Rodriguez-Berral, M. Garcia-Vigueras, F. Medina, and J. R. Mosig, *IEEE Transactions on Antennas and Propagation* **64**, 1106 (2015).
- [31] C. Molero, R. Rodriguez-Berral, F. Mesa, and F. Medina, *Physical Review E* **95**, 023303 (2017).
- [32] H. A. Haus, *Waves and Fields in Optoelectronics* (Prentice-Hall, 1984).
- [33] S. Fan and J. D. Joannopoulos, *Physical Review B* **65**, 235112 (2002).
- [34] W. Suh, Z. Wang, and S. Fan, *IEEE Journal of Quantum Electronics* **40**, 1511 (2004).
- [35] L. Maloratsky, *Passive RF and Microwave Integrated Circuits* (Elsevier, 2003).
- [36] M. Benzaouia, J. D. Joannopoulos, S. G. Johnson, and A. Karalis, arXiv:2105.01749 (2021).
- [37] Q. Li, T. Wang, Y. Su, M. Yan, and M. Qiu, *Optics Express* **18**, 8367 (2010).
- [38] C. W. Hsu, B. G. DeLacy, S. G. Johnson, J. D. Joannopoulos, and M. Soljacic, *Nano Letters* **14**, 2783 (2014).
- [39] J. S. Jensen and O. Sigmund, *Laser & Photonics Reviews* **5**, 308 (2011).
- [40] S. Molesky, Z. Lin, A. Y. Piggott, W. Jin, J. Vucković, and A. W. Rodriguez, *Nature Photonics* **12**, 659 (2018).
- [41] N. Aage and V. Egede Johansen, *International Journal for Numerical Methods in Engineering* **112**, 283 (2017).
- [42] M. A. Popović, C. Manolatu, and M. R. Watts, *Optics Express* **14**, 1208 (2006).
- [43] M. A. Al-Joumayly and N. Behdad, *IEEE Transactions on Antennas and Propagation* **59**, 4542 (2011).
- [44] M. Li, M. A. Al-Joumayly, and N. Behdad, *IEEE transactions on antennas and propagation* **61**, 1166 (2012).
- [45] S. B. Glybovski, S. A. Tretyakov, P. A. Belov, Y. S. Kivshar, and C. R. Simovski, *Physics Reports* **634**, 1 (2016).
- [46] This should not be confused with a symmetric S matrix, which holds for a *reciprocal* system.
- [47] J. D. Joannopoulos, S. G. Johnson, J. N. Winn, and R. D. Meade, *Photonic Crystals: Molding the Flow of Light*, 2nd ed. (Princeton University Press, 2008).
- [48] L. Maleki, A. Matsko, A. Savchenkov, and V. Ilchenko, *Optics Letters* **29**, 626 (2004).
- [49] É. Chéron, S. Félix, and V. Pagneux, *Physical Review Letters* **122**, 125501 (2019).
- [50] Comsol Multiphysics[®] v5.1, www.comsol.com, COMSOL AB, Stockholm, Sweden.
- [51] See Supplemental Material.
- [52] A. Ahmed, I. A. Goldthorpe, and A. K. Khandani, *Appl. Phys. Rev.* **2**, 011302 (2015).
- [53] O. Tsilipakos, T. Koschny, and C. M. Soukoulis, *ACS Photonics* **5**, 1101 (2018).
- [54] W. T. Chen, A. Y. Zhu, and F. Capasso, *Nat. Rev. Mat.* **5**, 604 (2020).
- [55] J. T. Conway, *IEEE Transactions on Magnetics* **43**, 1023 (2007).

Supplemental Material

I. QNM PARAMETERS FOR STRUCTURES

Here, we provide all the QNMs computed via finite-element simulations. The computed QNM-to-CPM ratios are indicated by σ . The modes used to calculate the background C matrix are marked in bold. Ω and Γ in the tables are in units of $\omega_c = 2\pi \times 10$ GHz.

We remind that good approximate solutions with complex $\gamma = e^{i\varphi}$ can be found, so we allow a common phase $\sqrt{\gamma}$ for the ratios σ during optimization. Deviations of the final computed $\sigma/\sqrt{\gamma}$ from the ideal ± 1 or $\pm i$ shown below lead to only small errors in the ISF designs. For symmetric structures, all computed σ are equal to ± 1 anyway. (Note that, after the design optimization process is completed, we do not care to fine-tune σ for QNMT modeling, since in Figs. 4,5 we only show the exact transmission spectra from direct frequency-domain simulations anyway.)

- Third-order bandpass filters of Fig. 6:

Type	Butterworth ($\varphi = 0$)			Chebyshev ($\varphi = 0$)			Inverse Chebyshev ($\varphi = -0.07\pi$)		
Ω	0.9774	1.0010	1.0210	0.9788	1.0009	1.0223	0.9728	0.9975	1.0254
Γ	0.0127	0.0251	0.0123	0.0079	0.0154	0.0075	0.0119	0.0341	0.0128
$\sigma/\sqrt{\gamma}$	1	-1	1	1	-1	1	-0.94+0.00i	1.05+0.02i	-0.98+0.03i

Type	Elliptic 2% ($\varphi = -0.066\pi$)			Elliptic 6% ($\varphi = -0.059\pi$)			Elliptic 10% ($\varphi = -0.075\pi$)		
Ω	0.9885	0.9995	1.0101	0.9718	0.9987	1.0274	0.9516	0.9972	1.0504
Γ	0.0032	0.0086	0.0028	0.0076	0.0218	0.0078	0.0124	0.0392	0.0145
$\sigma/\sqrt{\gamma}$	-1.04-0.14i	1.16+0.03i	-1.10+0.17i	-1.04+0.03i	0.91-0.01i	-1.01-0.04i	-1.04-0.15i	1.19+0.00i	-1.03+0.15i

- Third-order bandstop filter of Fig. 7(a): ($\varphi = -0.16\pi$)

Ω	0.949	1.004	1.065
Γ	0.0156	0.0809	0.0158
$\sigma/\sqrt{\gamma}$	0.95+0.04i	-0.97+0.00i	0.97-0.04i

- Second-order bandpass filter of Fig. 7(b):

Ω	0.738	0.751	0.996	1.004	1.186	1.191	1.289	1.362
Γ	0.297	0.301	0.0031	0.0031	0.0012	0.011	0.0084	0.0007
σ	1	-1	-1	1	-1	1	-1	1

The modes marked in bold lead to $|C_{21}(\omega_c)| = -24.9$ dB and $\beta = C_{11}C_{21}^*/|C_{11}C_{21}| = -i$.

- Second-order bandstop filter of Fig. 7(c):

Ω	0	0.954	1.042	1.109	1.459	1.481	1.892
Γ	0.851	0.0313	0.0343	0.993	0.0156	0.0024	0.945
σ	1	-1	1	-1	1	-1	1

Note that the ‘‘Fabry-Perot’’ modes here have such a large Γ that higher-order such modes will still have an effect at frequencies around $\omega \sim \omega_c$. However, they lie deep inside the diffraction zone, so they are hard to identify from spurious modes. Therefore, as explained in the main text, we calculated more accurately $C(\omega_c) = \bar{S}^{-1}(\omega_c)S(\omega_c)$, with \bar{S} and S obtained at ω_c from QNMT on the two high- Q modes and a direct computation respectively. The optimized result is then indeed $|C_{21}(\omega_c)| = -0.25$ dB and $\beta = i$.